

# Using Persistent Homology Topological Features to Characterize Medical Images: Case Studies on Lung and Brain Cancers

Chul Moon<sup>\*1</sup>, Qiwei Li<sup>2</sup>, and Guanghua Xiao<sup>3</sup>

<sup>1</sup>Department of Statistical Science, Southern Methodist University, Dallas, TX, USA

<sup>2</sup>Department of Mathematical Sciences, University of Texas at Dallas, Richardson, TX, USA

<sup>3</sup>Quantitative Biomedical Research Center, Department of Population & Data Sciences and Department of Bioinformatics, University of Texas Southwestern Medical Center, Dallas, TX, USA

## Abstract

Tumor shape is a key factor that affects tumor growth and metastasis. This paper proposes a topological feature computed by persistent homology to characterize tumor progression from digital pathology and radiology images and examines its effect on the time-to-event data. The proposed topological features are invariant to scale-preserving transformation and can summarize various tumor shape patterns. The topological features are represented in functional space and used as functional predictors in a functional Cox proportional hazards model. The proposed model enables interpretable inference about the association between topological shape features and survival risks. Two case studies are conducted using consecutive 143 lung cancer and 77 brain tumor patients. The results of both studies show that the topological features predict survival prognosis after adjusting clinical variables, and the predicted high-risk groups have significantly (at the level of 0.01) worse survival outcomes than the low-risk groups. Also, the topological shape features found to be positively associated with survival hazards are irregular and heterogeneous shape patterns, which are known to be related to tumor progression.

*Keywords: Topological Data Analysis, Tumor Shape, Functional Principal Component Analysis*

---

<sup>\*</sup>Corresponding author. Email: chulm@smu.edu

# 1 Introduction

Recent advancements in the field of medical imaging lead to a high-resolution and informative description of human cancer. The Artificial Intelligence (AI) image processing algorithms, such as deep learning, have been developed to extract information from medical images and attained comparable achievements with human experts (Havaei et al., 2017; Levine et al., 2019; Wang et al., 2019). These AI algorithms also enable efficient medical image segmentation, which classifies image patches into categories such as tumors and normal regions. With such developments, medical images have a significant influence on medical decision making. Radiomics has been developed for decision support by extracting quantitative features of images and providing data for further analyses (Gillies et al., 2016; Rizzo et al., 2018). The two of the most common types of features of tumors are texture and shape (Bianconi et al., 2018). The textural features summarize the area, kurtosis, entropy, and correlation computed from pixel intensity and the gray-level co-occurrence matrix (Haralick et al., 1973). The shape features mainly focus on the boundaries of segmented tumor regions and quantify their roughness or irregularities (Bharath et al., 2018; Brú et al., 2008; Kilday et al., 1993; Bookstein, 1997; Zhang et al., 2020; Crawford et al., 2020). However, the existing tumor shape features do not summarize detailed local patterns such as a relationship between tumor and normal regions, distribution, and connectivity. Also, the features developed to deal with radiographic images could be inadequate in high-resolution pathology images (Madabhushi and Lee, 2016; Zhang et al., 2020). In this paper, we propose using topological features computed by persistent homology to quantify various aspects of tumor shape features in the AI-segmented medical images.

Topological data analysis is a recently emerged area of study that investigates the shape of data using their topological features. Persistent homology is a commonly used topological data analysis tool that analyzes the shape of data with the multi-scale topological lens (Edelsbrunner and Harer, 2008; Carlsson, 2009). Persistent homology provides a numeric summary of the shape that is robust to noise and insensitive to metrics (Chazal et al., 2017). Persistent homology has been applied to various tumor image analyses (Qaiser et al., 2016; Lawson et al., 2019; Oyama et al., 2019; Berry et al., 2020) but their topological features are closer to the textural features than the shape features. Crawford et al. (2020) recently

propose topological features that represent a shape of tumor boundaries. However, their approach is sensitive to transformation, only analyzes an outer boundary of tumor regions, and the proposed model cannot handle censored data.

We propose topological shape features for medical images computed by persistent homology. We first develop the distance transform that can reveal the tumor shape of AI-segmented medical images. Persistent homology is computed based on the proposed distance transform values. Unlike the most existing shape features that only focus on a few large segmented tumor regions, the proposed approach quantifies all tumor patterns, such as shape, size, distribution, and connectivity. The proposed topological shape features are invariant to the scale-preserving transformation, such as rotation and translation, and applicable to various types of medical images, including pathology and radiology images.

Statistical inference on different tumor shapes and patterns in medical images can be achieved by using the proposed persistent homology shape features. However, persistent homology results cannot be used as predictors in most statistical models; 1) numeric outputs of persistent homology are sets of intervals that are not vectors, and 2) the number of intervals generated is different from dataset to dataset. Several methods have been suggested to represent persistent homology results in different spaces (Chen et al., 2015; Bendich et al., 2016; Kusano et al., 2016; Adams et al., 2017; Berry et al., 2020). In this paper, persistent homology results are represented in a functional space and implemented in a survival model as functional predictors.

We consider the Functional Cox Proportional Hazards model (FCoxPH) to characterize the association between functional topological shape features and survival outcomes. Since Chen et al. (2011) propose the FCoxPH model, various approaches have been developed (Gellar et al., 2015; Lee et al., 2015; Qu et al., 2016; Hao et al., 2020). In our study, the FCoxPH model of Kong et al. (2018) is extended to include multiple functional predictors obtained by persistent homology. The FCoxPH model implements both clinical variables and topological shape features and provides an interpretable result.

We conduct case studies on lung cancer pathology images and brain tumor Magnetic Resonance Imaging (MRI) images, both image data were collected as part of clinical routine procedures. The results show that the proposed shape features calculated from routine

medical images can be used to predict patient prognosis. The predicted high- and low-risk groups show significant differences in survival outcomes for both lung cancer pathology image dataset (p-value =  $3 \times 10^{-7}$  and hazard ratio = 5.462) and brain tumor MRI image applications (p-value = 0.0069 and hazard ratio = 1.971). We find that the irregular tumor shapes and heterogeneous patterns are positively related to risks of death, which coincide with the aggressive tumor patterns. The proposed method enables in-depth shape analysis on the survival prognosis using topological tumor shape features of medical images.

The rest of the paper is organized as follows. Section 2 introduces persistent homology and topological features of medical images as well as their functional representations. Section 3 describes the FCoxPH model. Section 4 presents applications to lung cancer pathology and brain tumor MRI image data. Section 5 concludes the paper and discusses future research topics.

## 2 Topological Shape Analysis for Medical Images

There are only a few studies that use topological features of medical images to predict patient survival outcomes. Recently, Crawford et al. (2020) use the Smooth Euler Characteristic Transform (SECT) to summarize the shape of the tumor boundary of glioblastoma multiforme (GBM) and predict the survival prognosis using Gaussian Process (GP) regression (see the supplementary materials for details). Although their approach suggests that the summary of tumor shape paired with its location becomes useful, it comes with several limitations. First, the GP regression model cannot handle the right-censored datasets. Second, the SECT is sensitive to the rotation and orientation of images. This is challenging for some cases when medical images do not have a pre-defined direction. Third, it is difficult to interpret the GP regression result and provide clinical implications. To overcome the challenges, we propose using persistent homology to describe the shape of medical images.

### 2.1 Homology and Persistent Homology

We first introduce a short theoretical background of topology to define topological shape features. Consider a shape is given as a topological space  $\mathcal{S}$ . Homology studies geometric

patterns of  $\mathcal{S}$  by examining its  $k$ -dimensional holes. For example, zero-dimensional holes are connected components, one-dimensional holes are loops, and two-dimensional holes are voids. These  $k$ -dimensional holes are often called the topological features of the shape. Let  $H_k(\mathcal{S})$  denotes the  $k$ -th homology group of  $\mathcal{S}$ . The Betti number  $\beta_k$  is the rank of  $H_k(\mathcal{S})$  and it counts the number of  $k$ -dimensional holes in  $\mathcal{S}$ .

Computing homology of topological space is challenging, albeit its simple concept. To overcome the computational issue, a topological space  $S$  is often approximated as a simplicial complex  $K$ . The simplicial complex is a finite set of simplices glued together. Examples of simplices are a point (0-simplex), line (1-simplex), triangle (2-simplex), and tetrahedron (3-simplex). The discretized representation of shape enables computationally efficient homology computation (Edelsbrunner and Harer, 2008).

Persistent homology provides multi-scale homology representation of topological spaces. Let  $\emptyset \subseteq K_0 \subseteq K_\epsilon \subseteq \dots \subseteq K_N$  be a non-decreasing sequence of simplicial complexes. Here, the inclusion  $\subseteq$  implies that a set of simplices on the left side of  $\subseteq$  is included on the right side of the simplicial complex. The index  $\epsilon$  that controls the sequence is called the filtration. The inclusion of  $K_i$  in  $K_j$  for  $0 \leq i \leq j \leq N$  induces a map between the homology groups so that  $0 \rightarrow H(K_0) \rightarrow H(K_1) \rightarrow \dots \rightarrow H(K_N)$ . The image of the map between homology groups includes information when a specific  $k$ -dimensional hole appears (birth) and disappears (death) over the filtration. Persistent homology computation result is given as multiple intervals of (birth, death). The length of the interval (death–birth) shows how long the topological feature persists.

A persistence diagram is a collection of points in  $\mathbb{R}^2$  where points in the diagram represent the birth and death values of features. Let  $P = \{(b, d) \in \mathbb{R}^2 : b < d\}$  be a persistence diagram such that  $(b, d)$  denotes the birth and death values and  $\mathcal{D}$  be the space of persistence diagrams. The birth and death values can be plotted as points on the horizontal and vertical axis, respectively. For more detailed explanation and examples of these concepts, see the supplementary materials.

## 2.2 Persistent Homology Shape Features of Medical Images

Persistent homology can reveal resourceful shape information when it is applied to image data. Especially, persistent homology applied to a signed distance transformed binary material images successfully reveals pore structures and networks (Robins et al., 2016; Moon et al., 2019). The signed distance transform used in Robins et al. (2016) cannot be used to the three-class images because it is suitable for binary images.

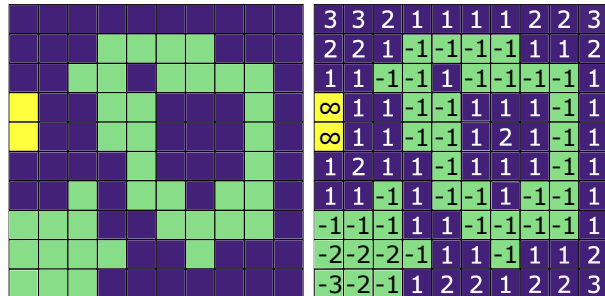
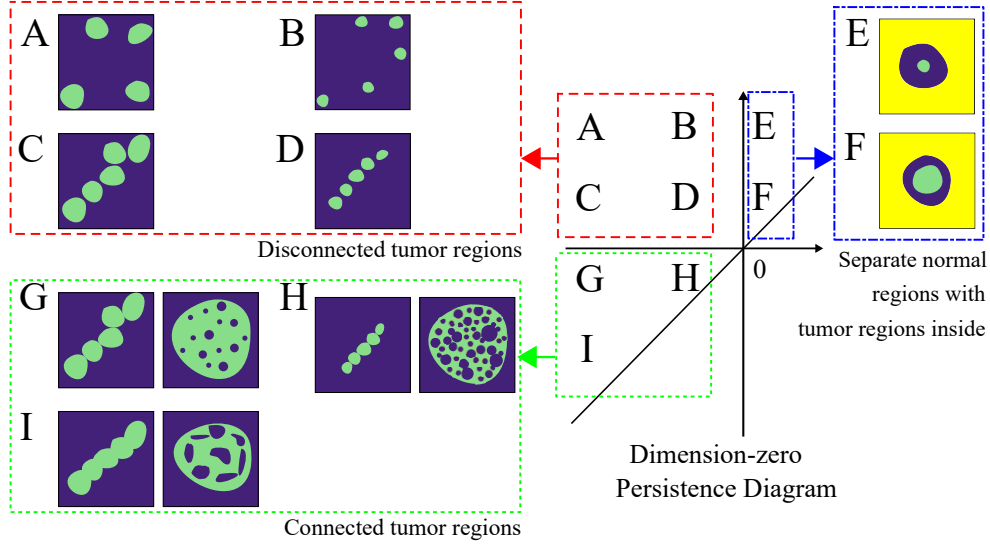


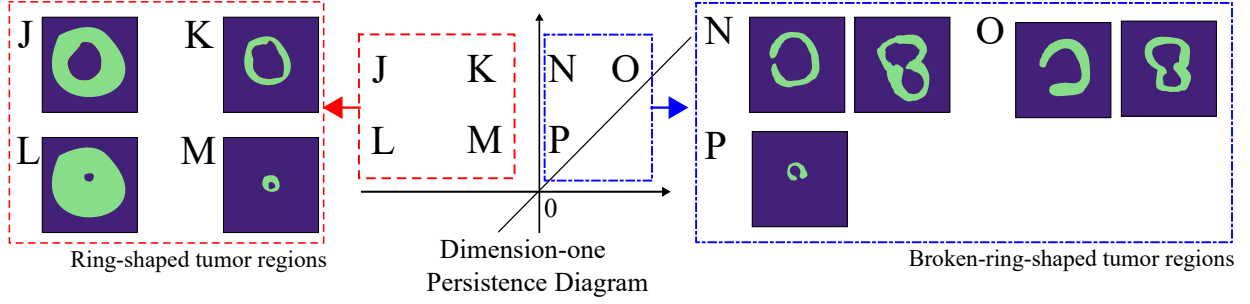
Figure 1: Three-class medical image example (left) and its signed distance assigned to each pixel using the taxicab distance (right). The green-, blue-, and yellow-colored pixels are tumor, normal, and empty regions, respectively.

We propose a Signed Euclidean Distance Transform for the three-class medical images (SED3T-3). Suppose that all pixels of medical images are classified into one of the three classes: tumor, normal, and empty regions. The three-class image itself does not reveal connectivity or size information. Structural and shape information can be discovered by using the distance transform. The proposed SED3T-3 assigns the shortest Euclidean distance to the other classes to each pixel. The sign of the SED3T-3 value depends on the classes; negative values for tumor region pixels, positive values for normal region pixels, and infinite values for the empty region pixels. The signed distance values have shape information in the sense that it shows connectivity and adjacency relationships between the neighboring pixels. Figure S3 presents the three-class medical image example and its signed distance transformed values. Here, a taxicab metric is used instead of a Euclidean distance for convenience.

We construct a cubical complex using the distance transform values to compute persistent homology. The cubical complex is a set of multi-dimensional cubes, such as points,



(a) Dimension-zero persistence diagram and the corresponding topological shape feature examples



(b) Dimension-one persistence diagram and corresponding topological shape feature examples

Figure 2: Interpretation of persistence diagrams of three-class medical images. The green, blue, and yellow colored pixels are tumor, normal, and empty regions, respectively.

lines, squares, and cubes, that are glued together. The cubical complex allows describing a structure of an image while preserving its topology (Couprie et al., 2001). We can obtain multi-scale shape information by computing persistent homology of the sequence of cubical complices. The empty regions are not used to construct cubical complices, so they do not directly affect persistent homology results. This is because the SEDT-3 assigns infinite value to empty region. See the supplementary materials for detailed illustrations of cubical complices persistent homology computation.

The proposed persistent homology approach can summarize various tumor shapes and they are recorded in different areas of persistence diagrams. Figure 2 illustrates the areas

of dimension-zero and dimension-one persistence diagrams and the examples of the shape features. See the supplementary materials for more detailed interpretation of the computed shape features.

The proposed topological shape features by persistent homology are invariant to scale-preserving transformations, which include rotation, translation, and reflection. Our features only depend on the relative locations between the nearest other phase-regions. Therefore, the proposed approach is automatically invariant to rotations and orientation shifts.

We note that the size of features is measured by the radius of the largest circle that can be placed inside of it. Also, dimension-zero and dimension-one features are not exclusive; the pixels used to construct dimension-zero features can be used to build dimension-one feature and vice versa. For example, tumor regions in Figure 2b are also counted as dimension-zero features.

### 2.3 Functional Representation of Persistent Homology Shape Features

Although persistence diagrams include topological persistence signal information, it is not easy to use them directly as input in data analysis. This is because persistence diagrams are not in a common data type that most statistical models use. In our study, we represent persistence diagrams as persistence functions in a functional space inspired by Chen et al. (2015) and Adams et al. (2017).

We define the persistence function  $\rho_P$  of the persistence diagram  $P$  as

$$\rho_P(x, y) = \sum_{(b,d) \in P} g_{(b,d)}(x, y) \cdot w(b, d),$$

where  $x$  and  $y$  are the  $(x, y)$ -coordinates of the persistence function,  $g_{(b,d)}$  is a smoothing function for  $(b, d) \in P$ , and  $w(b, d) \geq 0$  is a non-negative weight function. A persistence function is a stable representation of a persistence diagram; persistence functions are robust to small perturbations of points in persistence diagrams (Adams et al., 2017). Figure 3 illustrates a persistence diagram and its functional representation.

The weight function  $w(b, d)$  allows assigning different importance to points in persistence diagrams. For example, long-persisting features could be more important than the short-



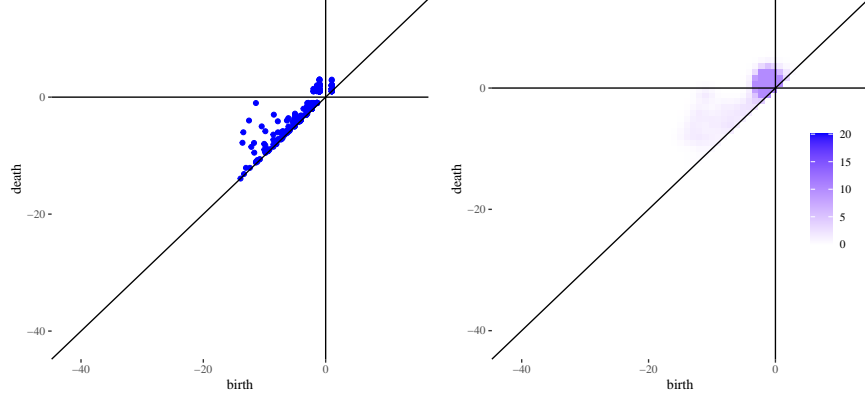


Figure 3: Persistence diagram (left) and persistence function (right).

living features in some applications. In this case, one can assign heavier weights to the points far from the diagonal. Various weights have been suggested, such as weights only depend on persistence of features (Chen et al., 2015; Adams et al., 2017; Kusano et al., 2016) and birth, death, and persistence values (Berry et al., 2020). In this paper, we use the maximum distance weight  $w(b, d) = \max\{|b|, |d|, d - b\}$  that assigns heavier weights to features far from the origin of persistence diagrams.

The persistence function is computed using the Gaussian smoothing function  $g_{(b,d)}(x, y) = \frac{\exp[-((x-b)^2 + (y-d)^2)]}{\sigma^2}$ . We modify the rule of thumb of Scott (2015) to select the smoothing bandwidth  $\sigma = (\frac{\sigma_b + \sigma_d}{2}) M_n^{-\frac{1}{6}}$ , where  $\sigma_b$  and  $\sigma_d$  are the standard deviations of birth and death values, respectively, and  $M_n$  is the median number of topological features obtained from medical images. For the two-dimensional medical images, two persistence functions will be obtained: dimension-zero and dimension-one. We denote persistence functions of dimension-zero and dimension-one diagrams of subject  $i$  by  $X_i^0$  and  $X_i^1$ , respectively.

### 3 Cox Regression Model for Functional Data

A Cox Proportional Hazards model (CoxPH) (Cox, 1972) is a commonly used model to investigate the association between patients' survival prognosis and predictor variables. The hazard function with a  $p$ -dimensional scalar predictor  $Z = (z_1, \dots, z_p)^T$  has the form

$$h(t) = h_0(t) \exp(Z^T \gamma), \quad (1)$$

where  $h_0$  is the baseline hazard function and  $t \in [0, \tau]$  for  $0 < \tau < \infty$ . We aim to conduct the FCoxPH model that uses a set of clinical predictor  $\gamma$  and two functional predictors  $X^0$  and  $X^1$  as

$$h(t) = h_0(t) \exp \left( Z^T \gamma + \int X^0(u) \alpha(u) du + \int X^1(v) \beta(v) dv \right). \quad (2)$$

The objective of the FCoxPH model is to determine the unknown coefficients  $\gamma$ ,  $\alpha$ , and  $\beta$ . Due to the infinite dimensionality of functional data, dimension reduction is often required. We use the functional principal component analysis to represent functional data in a lower-dimensional space as suggested in Kong et al. (2018).

We represent the persistence functions of medical image  $i$ ,  $X_i^0$  and  $X_i^1$ , with a few Functional Principal Components (FPC). Let  $\mu^0(u) = E[X_i^0(u)]$  and  $\mu^1(v) = E[X_i^1(v)]$  be the mean functions of  $X_i^0$  and  $X_i^1$ . By the spectral decomposition, the covariance functions can be represented as  $\text{Cov}(X_i^0(u), X_i^0(u')) = \sum_{j=1}^{\infty} \lambda_j \phi_j(u) \phi_j(u')$  and  $\text{Cov}(X_i^1(v), X_i^1(v')) = \sum_{k=1}^{\infty} \delta_k \pi_k(v) \pi_k(v')$  where  $\{\lambda_j\}_{j \geq 1}$  and  $\{\delta_k\}_{k \geq 1}$  are non-increasing eigenvalues and  $\{\phi_j\}_{j \geq 1}$  and  $\{\pi_k\}_{k \geq 1}$  are orthonormal eigenfunctions of  $X_i^0(u)$  and  $X_i^1(v)$ . By the Karhunen-Loève theorem, the persistence functions  $X_i^0$  and  $X_i^1$  can be expressed as

$$X_i^0(u) = \mu^0(u) + \sum_{j=1}^{\infty} \xi_{ij} \phi_j(u), \quad X_i^1(v) = \mu^1(v) + \sum_{k=1}^{\infty} \zeta_{ik} \pi_k(v),$$

where  $\xi_{ij} = \int (X_i^0(u) - \mu^0(u)) \phi_j(u) du$  and  $\zeta_{ik} = \int (X_i^1(v) - \mu^1(v)) \pi_k(v) dv$  are the FPCs of dimension-zero and dimension-one, respectively. The FPCs have mean zero  $E[\xi_{ij}] = E[\zeta_{ik}] = 0$  with covariances  $E[\xi_{ij} \xi_{ij'}] = \lambda_j 1(j = j')$  and  $E[\zeta_{ik} \zeta_{ik'}] = \delta_k 1(k = k')$  where  $1(\cdot)$  is an indicator function. We can approximate functional data  $X_i^0 \approx \mu^0(u) + \sum_{j=1}^q \xi_{ij} \phi_j(u)$  and  $X_i^1 \approx \mu^1(v) + \sum_{k=1}^r \zeta_{ik} \pi_k(v)$ , where  $q$  and  $r$  are the selected number of FPCs. Then the FCoxPH model (2) can be approximated as

$$h_i(t) \approx h_0^*(t) \exp \left( Z_i^T \gamma + \sum_{j=1}^q \xi_{ij} \alpha_j + \sum_{k=1}^r \zeta_{ik} \beta_k \right), \quad (3)$$

where  $h_0^*(t) = h_0(t) \exp \left( \int \mu^0(u) \alpha(u) du + \int \mu^1(v) \beta(v) dv \right)$ . The dimension of predictors is reduced to  $p + q + r$  in the FCoxPH model (3). We can obtain the estimated coefficients

using the selected FPCs and their estimated coefficients as  $\hat{\alpha}(u) \approx \sum_{j=1}^q \hat{\alpha}_j \hat{\phi}_j(u)$  and  $\hat{\beta}(v) \approx \sum_{k=1}^r \hat{\beta}_k \hat{\pi}_k(v)$ .

The FCoxPH model that incorporates the functional tumor shape predictors enables interpretable inference about the association between shape patterns and survival outcomes. The estimated functional coefficients  $\hat{\alpha}(u)$  and  $\hat{\beta}(v)$  inform which parts of persistence functions are associated with survival risks. The findings also can be presented by figures that plot the estimated coefficients on the space of a persistence function. By comparing the estimated coefficients plots and the shape features in Figure 2, one can see which shape patterns contribute the most to the hazard prediction.

Kong et al. (2018) suggest two criteria for selecting the number of FPCs for FCoxPH models. First, the percentage of variance explained by the FPCs can be used to determine  $q$  and  $r$ . Let  $PV^0(q) = \sum_{j=1}^q \lambda_j / \sum_{j=1}^{\infty} \lambda_j$  and  $PV^1(r) = \sum_{k=1}^r \delta_k / \sum_{k=1}^{\infty} \delta_k$  be the percentages of variances explained by  $q$  dimension-zero and  $r$  dimension-one FPCs, respectively. For a given variability threshold  $C$ , the minimum number of FPCs that exceed the threshold:  $q = \min\{q : PV^0(q) > C\}$  and  $r = \min\{r : PV^1(r) > C\}$ . Second, the Akaike information criterion (AIC) can be used to choose the number of the FPCs (Yao et al., 2005). Let  $L(\gamma_1, \dots, \gamma_p, \alpha_1, \dots, \alpha_q, \beta_1, \dots, \beta_r \mid q, r)$  denote the partial likelihood function of the FCoxPH (3) given the number of the FPCs  $q$  and  $r$ . The AIC value of the FCoxPH model is  $AIC(q, r) = 2(q + r) - 2 \log\{L(\hat{\gamma}_1, \dots, \hat{\gamma}_p, \hat{\alpha}_1, \dots, \hat{\alpha}_q, \hat{\beta}_1, \dots, \hat{\beta}_r \mid q, r)\}$ . We determine an optimal number of components  $q$  and  $r$  by computing the AIC under the various combinations of  $q$  and  $r$ . For the tied event times, we use the approximation method of Efron (1977) to adjust the partial likelihood.

## 4 Case Studies

### 4.1 Application to Lung Cancer Pathology Images

Lung cancer is one of the most deadly cancers (Siegel et al., 2020). One of the most common types of lung cancer is adenocarcinoma that accounts for about 40% of all lung cancers (Zappa and Mousa, 2016), and it has various morphological features (Matsuda and Machii,

2015). We use 246 pathology images of 143 lung adenocarcinoma patients in the National Lung Screening Trial (NLST) data. All images are obtained under  $40\times$  magnification, and the median size of images is  $24,244 \times 19,261$  pixels. The images are segmented into three classes of tumor, normal, and empty regions using a deep convolutional neural network (Wang et al., 2018). We implement an additional pre-processing step to remove noise. A single pixel is considered to be noise when its class is different from the surrounding eight singular-class pixels. The noise pixels are reclassified to the class of the surrounding pixels. The denoised three-class images are transformed using the SEDT-3. Figure 4 presents the denoised ternary image of Wang et al. (2018) and the SEDT-3 transformed image.

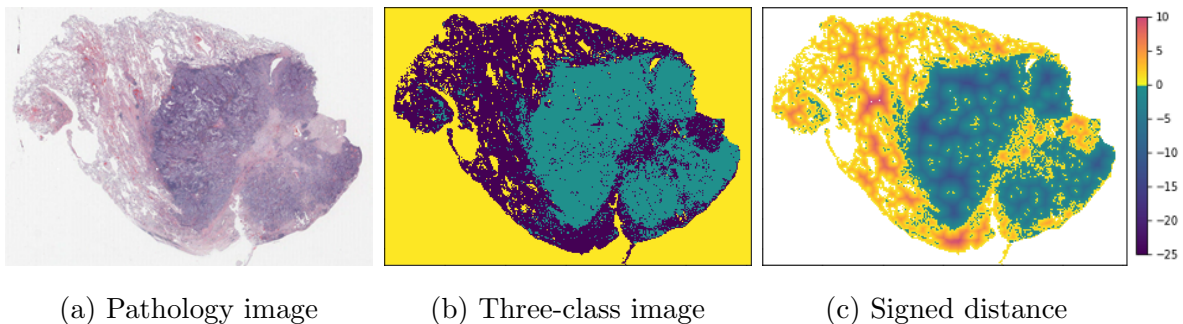


Figure 4: The lung adenocarcinoma pathology image (left), denoised three-class pathology image segmented by Wang et al. (2018) (middle), and signed Euclidean distance transformed image (right). In the ternary image, the green, blue, and yellow colored pixels are tumor, normal, and empty regions. In the signed distance transformed image, tumor regions are colored from blue to green and normal regions are colored yellow to red.

A sequence of cubical complices is constructed using the SEDT-3 value as filtration, and persistent homology is computed using GUDHI (Dlotko, 2015). We exclude the intervals with infinite death values to remove features related to empty regions. The median number of the computed features per image slice is 694 for dimension-zero and 1,768 for dimension-one. The ranges are  $(-41, 11)$  for dimension-zero and  $(-19, 26)$  for dimension-one persistence diagrams, respectively.

The computed persistence diagrams are represented as the persistence function using the Gaussian smoothing kernel with the maximum distance weight. We observe the persistence functions on grid points at the center of the square lattices of size one, on and above the

persistence diagram’s diagonal line. As a result, we use 1,378 and 1,035 grid points for the dimension-zero and dimension-one persistence functions, respectively.

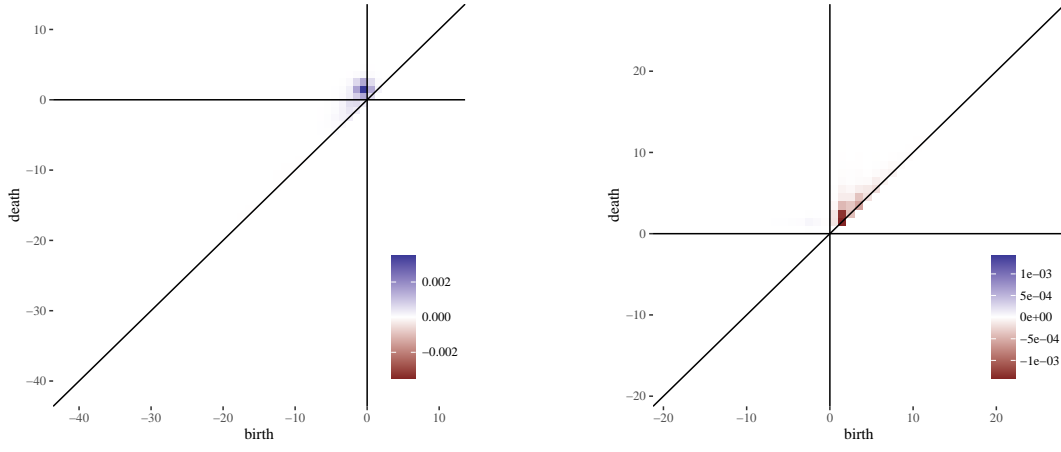
#### 4.1.1 Model Estimation

We construct the CoxPH model using the following scalar clinical predictors: age, sex, smoking status, stage of cancer (I to IV), and tumor size. The size of tumor is measured by the number of tumor pixels in an image slice. Also, we fit the FCoxPH model using the functional predictors and the same clinical predictors used in the CoxPH model. The persistence functions are represented by functional principal component analysis, and the selected FPCs are included in the FCoxPH model. The AIC criterion yield three selected FPCs: one FPC from dimension-zero ( $q = 1$ ) and two FPCS for dimension-one ( $r = 2$ ). For both models, we assume the baseline hazard function  $h_0(t) = 1$ . The CoxPH and FCoxPH models are fitted using the R-package “survival” (Therneau, 2020).

Table 1: The outputs of the Cox proportional hazards (CoxPH) and functional Cox proportional hazards (FCoxPH) models of the lung cancer adenocarcinoma patients. The ‘coef.’ and ‘SE’ are abbreviations of the coefficient and standard error, respectively. The p-values smaller than 0.05 are marked in bold.

	CoxPH model				FCoxPH model			
	coef.	exp(coef.)	SE	p-value	coef.	exp(coef.)	SE	p-value
Age	0.084	1.088	0.023	<b>0.007</b>	0.083	1.087	0.024	<b>0.013</b>
Smoker vs. non-smoker	-0.067	0.935	0.262	0.831	-0.253	0.776	0.234	0.426
Female vs. male	0.081	1.085	0.235	0.803	0.088	1.092	0.242	0.791
Tumor size	0.000	1.000	0.000	0.084	<0.001	1.000	<0.001	0.572
Stage II vs. stage I	0.545	1.725	0.382	0.366	0.477	1.611	0.390	0.432
Stage III vs. stage I	1.195	3.304	0.270	<b>0.002</b>	1.170	3.222	0.277	<b>0.002</b>
Stage IV vs. stage I	1.442	4.227	0.342	<b>0.002</b>	1.424	4.152	0.346	<b>0.003</b>
Dimension 0, 1 <sup>st</sup> FPC	-	-	-	-	0.005	1.005	0.001	< <b>0.001</b>
Dimension 1, 1 <sup>st</sup> FPC	-	-	-	-	<0.001	1.001	<0.001	<b>0.002</b>
Dimension 1, 2 <sup>nd</sup> FPC	-	-	-	-	-0.002	0.998	<0.001	< <b>0.001</b>

Table 1 shows the results of the CoxPH and FCoxPH models. Among the clinical predictors in both models, age and stage III and IV indicators have the p-values smaller than 0.05. In the FCoxPH model, the p-values of all FPCs are smaller than 0.05. The overall p-values of the Wald tests are  $2 \times 10^{-4}$  for the CoxPH model and  $1 \times 10^{-7}$  for the FCoxPH model. The clinical variables behave similarly for both models except for the tumor size predictor. The p-value of the tumor size variable is increased in the FCoxPH model as the functional predictors are included suggesting that one of the functional predictors may include the tumor size information. We conduct the chi-square test to check the validity of topological features for predicting the survival outcome. The test result (p-value =  $1 \times 10^{-13}$ ) indicates that the topological features are a strong signal (see the supplementary materials for further details).



(a) Dimension-zero functional coefficient  $\hat{\alpha}(u)$  (b) Dimension-one functional coefficient  $\hat{\beta}(v)$

Figure 5: Estimated coefficient functions  $\hat{\alpha}(u)$  and  $\hat{\beta}(v)$  of the functional Cox proportional hazards (FCoxPH) model of the lung adenocarcinoma patients. The estimated coefficient functions are plotted on the spaces of the dimension-zero and dimension-one persistence diagrams.

The estimated coefficients of persistence functions,  $\hat{\alpha}(u)$  and  $\hat{\beta}(v)$ , show which shape features affect the survival prognosis and how they are related. Figure 5 shows the estimated functional coefficients. The blue-colored and red-colored areas have positive and negative effects on the hazard function, respectively.

The topological features recorded in the blue-colored areas on the quadrant II and III of

Figure 5a correspond to the aggressive tumor patterns. First, the colored area in quadrant II in Figure 5a represents the small-sized scattered tumor regions close to each other (i.e., see the example of area D in Figure 2a). Also, quadrant III of Figure 5a represents the relatively small connected tumor shapes. The small connected tumor features are spotted where multiple tumor regions spread inside normal (i.e., see the examples of area H in Figure 2a). These patterns imply a fast spread of tumors.

On the other hand, the shapes appear in the red-colored regions in quadrant I of Figure 5b match with less aggressive tumor behaviors. The red-colored region corresponds to broken-ring shaped tumor regions (i.e., see the examples of areas N, P, and O in Figure 2b). These shapes require an ample-sized normal region that could be surrounded by tumor but not invaded by tumor. If a small tumor region penetrates the normal region inside the broken-ring shaped tumor regions, the dimension-one features are not constructed. Therefore, the broken-ring shaped tumor may not likely to appear where the small tumor regions are densely populated. These results coincide with the findings that tumor shape complexity and heterogeneous spread are associated with prognosis (Yokoyama et al., 1991; Miller et al., 2003; Chatzistamou et al., 2010; Vogl et al., 2013; Grove et al., 2015) and tissue transport properties (Soltani and Chen, 2012; Sefidgar et al., 2014).

Another interesting observation is that the relatively small-sized (approximately up to  $15 \times 15$  pixels) topological features have large effects on the hazard function. We see that most colored regions, the non-zero estimated coefficient areas, in Figure 5 are close to the origin compared to the ranges of persistence functions. The topological features near the origin correspond to small-sized features that have small birth and death values. This indicates that valuable information about the lung cancer patients obtained by the proposed persistent homology approach is mainly about local shapes and patterns.

#### 4.1.2 Prediction using Cross-validation

We predict the risk scores using the leave-one-out cross-validation (LOOCV) for two models, the CoxPH model (1) and the FCoxPH model (3). For a given pathology image  $I \in \{1, 2, \dots, 246\}$ , the models are trained for the rest 245 images. The risk score of  $I$  is predicted using the trained model. We repeat it for all 246 images, and the predicted risk

scores are averaged for each patient. We assign 143 patients into two groups of 71 high-risk patients and 72 low-risk patients using the median patient-wise risk score.

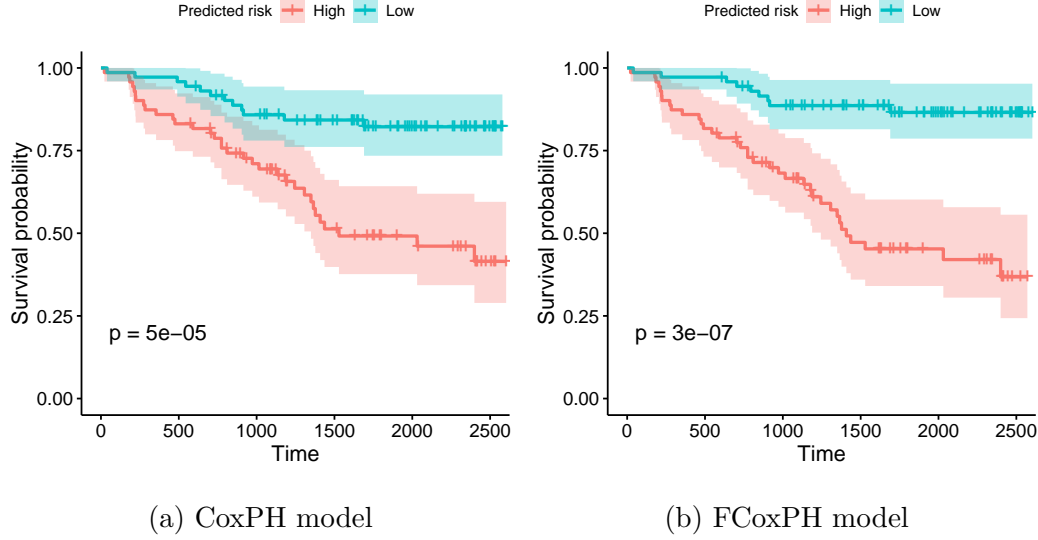


Figure 6: The Kaplan–Meier plots for the high- and low-risk groups of the Cox proportional hazards (CoxPH) and functional Cox proportional hazards (FCoxPH) models of the lung adenocarcinoma patients.

The proposed FCoxPH model shows a better separation between the two groups over the CoxPH model. The Kaplan-Meier plots of the high- and low-risk groups predicted by the two models are presented in Figure 6. The p-value of the log-rank test of the FCoxPH model is  $3 \times 10^{-7}$ , which is smaller than that of the CoxPH model  $5 \times 10^{-5}$ . The hazard ratios between the predicted high-risk group and the low-risk group of the FCoxPH and CoxPH models are 5.462 and 3.566, respectively.

Note that Crawford et al. (2020)’s method is not used in the lung pathology image study. The SECT is sensitive to the rotation and location, making it unsuitable for pathology images. Also, about 69% of observations are right-censored (98 out of 143 patients), so the outcome of the GP model, which cannot consider censoring, is not reliable.

## 4.2 Application to Brain Tumor MRI Images

GBM is the most common malignant grade IV brain tumor (Surawicz et al., 1999). GBM is distinguished from the lower-grade astrocytomas (grade II and III) by its accelerated



growth rate. The rapid outward growth of GBM develops necrosis, and it is considered a hallmark of GBM. On T1-weighted contrast-enhanced imaging MRI, most GBM cases show a ring-shaped enhancement made of hypervascular tissues with a necrotic region at the center (Zhu et al., 2000; Henson et al., 2005). Figure 7 shows the MRI image of the GBM patient that has a ring-enhancing mass. The presence of necrosis is a significant prognosis factor (Nelson et al., 1983), and clinical studies show that the degree of necrosis is negatively associated with a survival rate (Hammoud et al., 1996; Raza et al., 2002). However, due to its irregular shape, multifocal enhancement, and the existence of multiple small lesions, evaluation of GBM shapes using MRI images could be difficult (Eisenhauer et al., 2009; Upadhyay and Waldman, 2011).

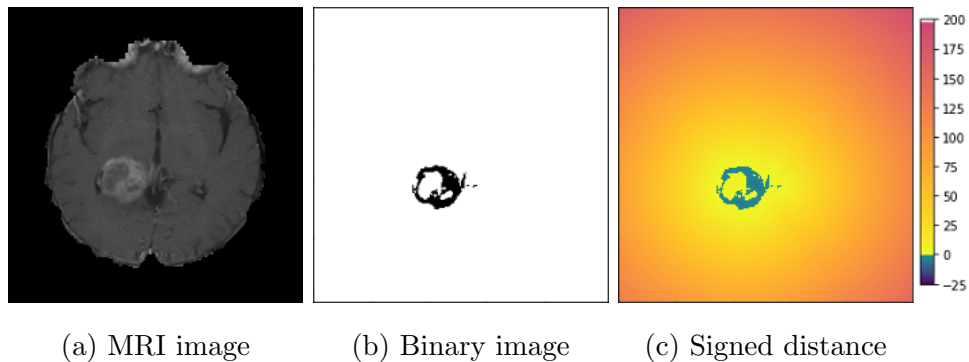


Figure 7: The T1-weighted contrast-enhanced MRI image of GBM patient (left), segmented binary image (middle), and signed distance transformed image (right). In the signed distance transformed image, the tumor regions are colored from blue to green and the normal regions are colored yellow to red.

We use 77 GBM patients’ MRI scans obtained from The Cancer Imaging Archive (TCIA) (Clark et al., 2013; Scarpance et al., 2016) and their clinical data retrieved from The Cancer Genome Atlas (TCGA) (Network et al., 2008). The MRI images are segmented into two classes of the tumor and non-tumor regions using the Medical Imaging Interaction Toolkit with augmented tools for segmentation (Chen and Rabadán, 2017). Each patient has approximately 23 to 25 segmented MRI slices and the spaces between the MRI slices are not the same. We only use the MRI images that have more than 100 tumor pixels because some images do not include tumor regions. The segmented binary images are transformed by the SEDT for two-class (SEDT-2). SEDT-2 is a simpler version of

SED3 that does not assign infinite values because the binary images do not have empty regions. Figures 7b and 7c show the segmented and signed distance transformed images.

The topological shape features in the MRI images are obtained by computing persistent homology of cubical complex based on the SED2 values. We use the same analytic pipeline used in Section 4. We represent the topological shape features as persistence functions and use the mean persistence function for each patient. Interpretation of the topological shape features of the binary images are similar to those of the three-class images illustrated in Figure 2; there are no topological features that summarize the separate non-tumor regions (e.g., E and F in Figure 2a).

The number of topological shape features of the GBM images are much smaller than the lung cancer pathology images. The median of the number of computed topological features per image slice is 16 for dimension-zero and 17 for dimension-one, respectively. The GBM tumors are scanned in smaller and simpler shapes compared to the lung cancer pathology images. This is because the MRI images are obtained in relatively lower-resolution than the pathology images. The ranges of topological shape summaries are  $(-22, 29)$  for dimension-zero and  $(-6, 35)$  for dimension-one persistence diagrams, respectively.

Note that the ring-shaped enhancements in MRI images of GBM patients are recorded as dimension-one topological shape features. As illustrated in Figure 2b, the broken-ring- and unbroken-ring-shaped masses appear in quadrant I and II of the dimension-one persistence diagram, respectively.

#### 4.2.1 Model Estimation

We fit the CoxPH and FCoxPH models to predict overall survival of the GBM patients. For both models, three clinical predictors are used: age, gender, and Karnofsky performance score (KPS). In the FCoxPH model, four FPCs (one dimension-zero ( $q = 1$ ) and three dimension-one FPCs ( $r = 3$ )) are selected by AIC.

Table 2 summarizes the results of the CoxPH and FCoxPH models. In both models, age has the p-value smaller than 0.05. In the FCoxPH model, the p-value of the one FPC is smaller than 0.05. The overall p-values of the Wald tests are 0.02 for the CoxPH model and  $6 \times 10^{-4}$  for the FCoxPH model. The p-value of the KPS in the FCoxPH model is

Table 2: The outputs of the Cox proportional hazards (CoxPH) and functional Cox proportional hazards (FCoxPH) models of glioblastoma multiforme patients. The ‘KPS’, ‘coef.’, and ‘SE’ are abbreviations of the Karnofsky performance score, coefficient, and standard error, respectively. The p-values smaller than 0.05 are marked in bold.

	CoxPH model				FCoxPH model			
	coef.	exp(coef.)	SE	p-value	coef.	exp(coef.)	SE	p-value
Age	0.030	1.030	0.013	<b>0.024</b>	0.035	1.036	0.013	<b>0.006</b>
Female vs. male	-0.030	0.744	0.311	0.340	-0.345	0.708	0.312	0.269
KPS	-0.021	0.980	0.010	<b>0.048</b>	-0.009	0.991	0.011	0.454
Dimension 0, 1st FPC	-	-	-	-	0.002	1.002	0.117	0.990
Dimension 1, 1st FPC	-	-	-	-	0.161	1.175	0.115	0.163
Dimension 1, 2nd FPC	-	-	-	-	0.045	1.175	0.084	0.597
Dimension 1, 3rd FPC	-	-	-	-	-0.305	0.737	0.128	<b>0.018</b>

increased compared to that of the CoxPH model, implying that the functional topological shape predictors may be correlated with the KPS. Also, the result of the chi-square test for examining validity of topological features ( $p\text{-value} = 2 \times 10^{-4}$ ) suggests that the proposed topological shape features are informative after adjusting the clinical variables (see the supplementary materials for details).

Figure 8 presents the estimated coefficient of dimension-one persistence function  $\hat{\beta}$  of the GBM patients. The blue-colored areas indicate that a larger number of small- and large-sized broken-ring-shaped features are associated with higher risks. These patterns are most likely to correspond to the large necrotic center and heterogeneous enhancement outside of the rim. On the other hand, the medium-sized dimension-one topological shape features are related to the lower hazards. The estimated coefficient of dimension-zero persistence function  $\hat{\alpha}$  is not presented because it is not significant.

#### 4.2.2 Prediction using Cross-validation

We compare the prediction results of three models: CoxPH, FCoxPH, and the GP model of Crawford et al. (2020). For the CoxPH and FCoxPH models, we obtain the predicted

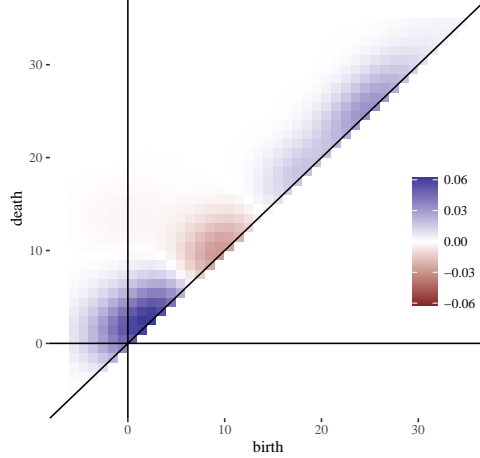


Figure 8: Estimated dimension-one coefficient function  $\hat{\beta}(v)$  of the functional Cox proportional hazards (FCoxPH) model of the GBM patients. The estimated coefficient function is plotted on the space of the dimension-one persistence diagram.

risk scores by using the LOOCV and designate high- and low-risk groups of 38 and 39 patients, respectively. Unlike the CoxPH and FCoxPH models, the GP model predicts the standardized survival times of patients, and does not provide risk information. Therefore, we compute the predicted standardized survival times for the GP model by the LOOCV and assign 38 and 39 patients to the shorter- and longer-surviving groups, respectively. Since the GP model does not consider clinical predictors, only the topological shape summary obtained by the SECT is used as predictors. Also, we use the Gaussian kernel in the GP model because it performs the best to predict overall survival (Crawford et al., 2020). We want to note that the six right-censored observations are used as an death time in the GP model because the model cannot handle the right-censored observations.

Figure 9 shows the Kaplan-Meier plots of the shorter- and longer-predicted surviving groups of the GP model and the high- and low-risk groups of the CoxPH and FCoxPH models. The p-values of the log-rank tests are 0.61 for the GP regression model, 0.17 for the CoxPH model, and 0.0069 for the FCoxPH model. The log-rank tests imply that the topological shape features captured by the proposed persistent homology framework provide a strong signal in predicting overall survival prognosis of the GBM patients after taking into account the clinical predictors. The hazard ratio between the predicted high-risk and low-risk groups is 1.437 for the CoxPH model and 1.971 for the FCoxPH model.

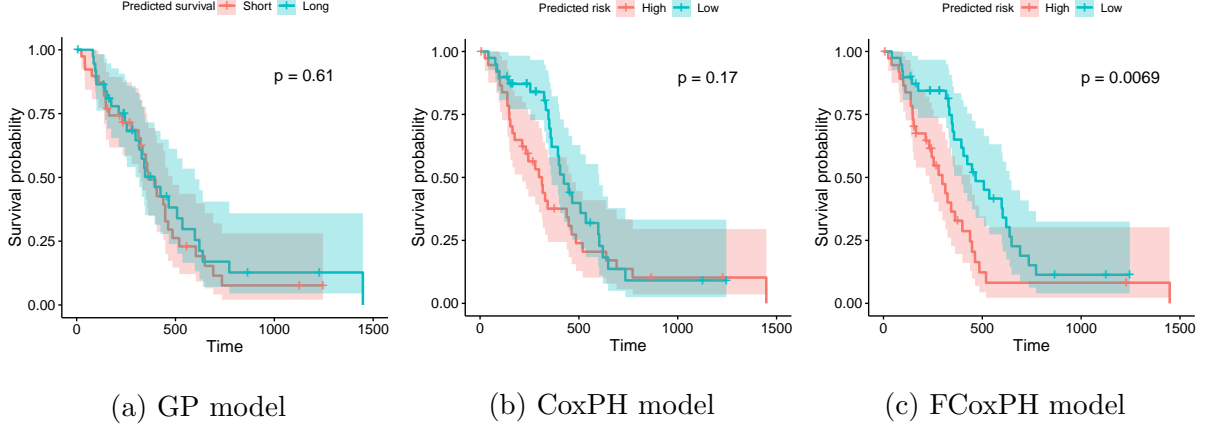


Figure 9: The Kaplan–Meier plots for the shorter- and longer-surviving groups of the Gaussian process (GP) model and the high- and low-risk groups of Cox proportional hazards (CoxPH), and functional Cox proportional hazards (FCoxPH) models of the GBM patients.

## 5 Conclusion

In this article, we propose a new summary statistic to represent the shape of tumors of medical images using their topological features. We develop the distance transform for three-class pathology and two-class radiology images to reveal various tumor patterns. We use persistent homology to quantify shape information and provide potential clinical interpretation of computed topological features. The topological persistence information is represented as functional data and used to fit the FCoxPH model to predict the survival prognosis of lung adenocarcinoma and GBM patients. The topological features are shown to have a significant non-zero effect on the hazard function. Also, the topological signals included in the FCoxPH model improve the predictive accuracy over the CoxPH model. This suggests that the proposed topological features well summarize tumor aggressiveness.

Our study leads to several interesting topics for future research. First, while we found a relationship between the topological shape features and survival prognosis, a complex relationship between the shape features, clinical variables, and genetic features are largely unknown. Recent studies investigate the relationships between imaging features and gene expressions; using the radiomic features of pancreatic ductal adenocarcinoma (Li et al., 2019) and the degree of tumor eccentricity of breast cancer (Moon et al., 2015). The future

research topic will include exploring the association of topological shape features with gene expressions. Also, one of the drawbacks of the proposed persistent homology approach is that it loses tumor location information. This is suitable for the lung adenocarcinoma application that the images do not have a pre-determined direction. However, the tumor spatial information could be important in some cancer image analyses, such as brain tumor (Bondy et al., 2008). In the future, it would be useful to pair spatial information with the topological features computed by persistent homology.

## Data Availability

Three examples of NLST lung cancer pathology images of Wang et al. (2018) are available from the repository <https://github.com/chulmoon/TopologicalTumorShape> and the binary GBM MRI images are available from the repository <https://github.com/lorinanthony/SECT>.

## Software Availability

Software is publicly available in Python (persistent homology computation) and R (functional representation and modeling) code, and located on the repository <https://github.com/chulmoon/TopologicalTumorShape>.

## Declaration of Interests

The authors declare that they have no conflict of interest.

## References

Adams, H., Emerson, T., Kirby, M., Neville, R., Peterson, C., Shipman, P., Chepushtanova, S., Hanson, E., Motta, F., and Ziegelmeier, L. (2017), “Persistence Images: A Stable Vector Representation of Persistent Homology,” *Journal of Machine Learning Research*, 18, 1–35.

- Bendich, P., Chin, S. P., Clark, J., Desena, J., Harer, J., Munch, E., Newman, A., Porter, D., Rouse, D., Strawn, N., and Watkins, A. (2016), “Topological and statistical behavior classifiers for tracking applications,” *IEEE Transactions on Aerospace and Electronic Systems*, 52, 2644–2661.
- Berry, E., Chen, Y.-C., Cisewski-Kehe, J., and Fasy, B. T. (2020), “Functional summaries of persistence diagrams,” *Journal of Applied and Computational Topology*, 4, 211–262.
- Bharath, K., Kurtek, S., Rao, A., and Baladandayuthapani, V. (2018), “Radiologic image-based statistical shape analysis of brain tumours,” *Journal of the Royal Statistical Society: Series C (Applied Statistics)*, 67, 1357–1378.
- Bianconi, F., Fravolini, M. L., Bello-Cerezo, R., Minestrini, M., Scialpi, M., and Palumbo, B. (2018), “Evaluation of shape and textural features from CT as prognostic biomarkers in non-small cell lung cancer,” *Anticancer research*, 38, 2155–2160.
- Bondy, M. L., Scheurer, M. E., Malmer, B., Barnholtz-Sloan, J. S., Davis, F. G., Il’Yasova, D., Kruchko, C., McCarthy, B. J., Rajaraman, P., Schwartzbaum, J. A., et al. (2008), “Brain tumor epidemiology: consensus from the Brain Tumor Epidemiology Consortium,” *Cancer*, 113, 1953–1968.
- Bookstein, F. L. (1997), *Morphometric tools for landmark data: geometry and biology*, Cambridge University Press.
- Brú, A., Casero, D., De Franciscis, S., and Herrero, M. A. (2008), “Fractal analysis and tumour growth,” *Mathematical and Computer Modelling*, 47, 546–559.
- Carlsson, G. (2009), “Topology and data,” *Bulletin of the American Mathematical Society*, 46, 255–308.
- Chatzistamou, I., Rodriguez, J., Jouffroy, T., Girod, A., Point, D., Sklavounou, A., Kittas, C., Sastre-Garau, X., and Klijanienko, J. (2010), “Prognostic significance of tumor shape and stromal chronic inflammatory infiltration in squamous cell carcinomas of the oral tongue,” *Journal of Oral Pathology & Medicine*, 39, 667–671.

- Chazal, F., Fasy, B., Lecci, F., Michel, B., Rinaldo, A., Rinaldo, A., and Wasserman, L. (2017), “Robust Topological Inference: Distance to a Measure and Kernel Distance,” *Journal of Machine Learning Research*, 18, 5845–5884.
- Chen, A. X. and Rabadán, R. (2017), “A fast semi-automatic segmentation tool for processing brain tumor images,” in *Towards Integrative Machine Learning and Knowledge Extraction*, Springer, pp. 170–181.
- Chen, K., Chen, K., Müller, H.-G., and Wang, J.-L. (2011), “Stringing high-dimensional data for functional analysis,” *Journal of the American Statistical Association*, 106, 275–284.
- Chen, Y.-C., Wang, D., Rinaldo, A., and Wasserman, L. (2015), “Statistical Analysis of Persistence Intensity Functions,” *arXiv e-prints*.
- Clark, K., Vendt, B., Smith, K., Freymann, J., Kirby, J., Koppel, P., Moore, S., Phillips, S., Maffitt, D., Pringle, M., et al. (2013), “The Cancer Imaging Archive (TCIA): maintaining and operating a public information repository,” *Journal of digital imaging*, 26, 1045–1057.
- Couprie, M., Bezerra, F.-N., and Bertrand, G. (2001), “Topological operators for grayscale image processing,” *Journal of Electronic Imaging*, 10, 1003 – 1015.
- Cox, D. R. (1972), “Regression Models and Life-Tables,” *Journal of the Royal Statistical Society. Series B (Methodological)*, 34, 187–220.
- Crawford, L., Monod, A., Chen, A. X., Mukherjee, S., and Rabadán, R. (2020), “Predicting clinical outcomes in glioblastoma: an application of topological and functional data analysis,” *Journal of the American Statistical Association*, 115, 1139–1150.
- Dlotko, P. (2015), “Cubical complex,” in *GUDHI User and Reference Manual*, GUDHI Editorial Board.
- Edelsbrunner, H. and Harer, J. (2008), “Persistent Homology - a Survey,” *Contemporary mathematics*, 453, 257–282, *Surveys on Discrete and Computational Geometry: Twenty Years Later*. Providence, IMS.



- Efron, B. (1977), “The Efficiency of Cox’s Likelihood Function for Censored Data,” *Journal of the American Statistical Association*, 72, 557–565.
- Eisenhauer, E. A., Therasse, P., Bogaerts, J., Schwartz, L. H., Sargent, D., Ford, R., Dancey, J., Arbuck, S., Gwyther, S., Mooney, M., et al. (2009), “New response evaluation criteria in solid tumours: revised RECIST guideline (version 1.1),” *European journal of cancer*, 45, 228–247.
- Gellar, J. E., Colantuoni, E., Needham, D. M., and Crainiceanu, C. M. (2015), “Cox regression models with functional covariates for survival data,” *Statistical Modelling*, 15, 256–278.
- Gillies, R. J., Kinahan, P. E., and Hricak, H. (2016), “Radiomics: images are more than pictures, they are data,” *Radiology*, 278, 563–577.
- Grove, O., Berglund, A. E., Schabath, M. B., Aerts, H. J., Dekker, A., Wang, H., Velazquez, E. R., Lambin, P., Gu, Y., Balagurunathan, Y., et al. (2015), “Quantitative computed tomographic descriptors associate tumor shape complexity and intratumor heterogeneity with prognosis in lung adenocarcinoma,” *PloS one*, 10, e0118261.
- Hammoud, M. A., Sawaya, R., Shi, W., Thall, P. F., and Leeds, N. E. (1996), “Prognostic significance of preoperative MRI scans in glioblastoma multiforme,” *Journal of neuro-oncology*, 27, 65–73.
- Hao, M., Liu, K.-y., Xu, W., and Zhao, X. (2020), “Semiparametric Inference for the Functional Cox Model,” *Journal of the American Statistical Association*, 1–11.
- Haralick, R. M., Shanmugam, K., and Dinstein, I. (1973), “Textural Features for Image Classification,” *IEEE Transactions on Systems, Man, and Cybernetics*, SMC-3, 610–621.
- Havaei, M., Davy, A., Warde-Farley, D., Biard, A., Courville, A., Bengio, Y., Pal, C., Jodoin, P.-M., and Larochelle, H. (2017), “Brain tumor segmentation with deep neural networks,” *Medical image analysis*, 35, 18–31.
- Henson, J. W., Gaviani, P., and Gonzalez, R. G. (2005), “MRI in treatment of adult gliomas,” *The lancet oncology*, 6, 167–175.

- Kilday, J., Palmieri, F., and Fox, M. D. (1993), “Classifying mammographic lesions using computerized image analysis,” *IEEE transactions on medical imaging*, 12, 664–669.
- Kong, D., Ibrahim, J. G., Lee, E., and Zhu, H. (2018), “FLCRM: Functional linear cox regression model,” *Biometrics*, 74, 109–117.
- Kusano, G., Hiraoka, Y., and Fukumizu, K. (2016), “Persistence weighted Gaussian kernel for topological data analysis,” *Proceedings of The 33rd International Conference on Machine Learning*, 48, 2004–2013.
- Lawson, P., Sholl, A., Brown, J., Fasy, B. T., and Wenk, C. (2019), “Persistent Homology for the Quantitative Evaluation of Architectural Features in Prostate Cancer Histology,” *Scientific Reports*, 9, 1139.
- Lee, E., Zhu, H., Kong, D., Wang, Y., Sullivan Giovanello, K., Ibrahim, J. G., and Neuroimaging Initiative, f. t. A. D. (2015), “BFLCRM: A Bayesian functional linear Cox regression model for predicting time to conversion to Alzheimer’s disease,” *Annals of Applied Statistics*, 9, 2153–2178.
- Levine, A. B., Schlosser, C., Grewal, J., Coope, R., Jones, S. J., and Yip, S. (2019), “Rise of the machines: advances in deep learning for cancer diagnosis,” *Trends in cancer*, 5, 157–169.
- Li, K., Xiao, J., Yang, J., Li, M., Xiong, X., Nian, Y., Qiao, L., Wang, H., Eresen, A., Zhang, Z., et al. (2019), “Association of radiomic imaging features and gene expression profile as prognostic factors in pancreatic ductal adenocarcinoma,” *American journal of translational research*, 11, 4491.
- Madabhushi, A. and Lee, G. (2016), “Image analysis and machine learning in digital pathology: Challenges and opportunities,” *Medical image analysis*, 33, 170–175.
- Matsuda, T. and Machii, R. (2015), “Morphological distribution of lung cancer from Cancer Incidence in Five Continents Vol. X,” *Japanese Journal of Clinical Oncology*, 45, 404–404.

- Miller, T. R., Pinkus, E., Dehdashti, F., and Grigsby, P. W. (2003), “Improved prognostic value of 18F-FDG PET using a simple visual analysis of tumor characteristics in patients with cervical cancer,” *Journal of Nuclear Medicine*, 44, 192–197.
- Moon, C., Mitchell, S. A., Heath, J. E., and Andrew, M. (2019), “Statistical inference over persistent homology predicts fluid flow in porous media,” *Water Resources Research*, 55, 9592–9603.
- Moon, H.-G., Kim, N., Jeong, S., Lee, M., Moon, H., Kim, J., Yoo, T.-K., Lee, H.-B., Kim, J., Noh, D.-Y., et al. (2015), “The clinical significance and molecular features of the spatial tumor shapes in breast cancers,” *PloS one*, 10, e0143811.
- Nelson, J., Tsukada, Y., Schoenfeld, D., Fulling, K., Lamarche, J., and Peress, N. (1983), “Necrosis as a prognostic criterion in malignant supratentorial, astrocytic gliomas,” *Cancer*, 52, 550–554.
- Network, C. G. A. R. et al. (2008), “Comprehensive genomic characterization defines human glioblastoma genes and core pathways,” *Nature*, 455, 1061.
- Oyama, A., Hiraoka, Y., Obayashi, I., Saikawa, Y., Furui, S., Shiraishi, K., Kumagai, S., Hayashi, T., and Kotoku, J. (2019), “Hepatic tumor classification using texture and topology analysis of non-contrast-enhanced three-dimensional T1-weighted MR images with a radiomics approach,” *Scientific Reports*, 9, 1–10.
- Qaiser, T., Sirinukunwattana, K., Nakane, K., Tsang, Y.-W., Epstein, D., and Rajpoot, N. (2016), “Persistent Homology for Fast Tumor Segmentation in Whole Slide Histology Images,” *Procedia Computer Science*, 90, 119 – 124.
- Qu, S., Wang, J.-L., and Wang, X. (2016), “Optimal estimation for the functional Cox model,” *Ann. Statist.*, 44, 1708–1738.
- Raza, S. M., Lang, F. F., Aggarwal, B. B., Fuller, G. N., Wildrick, D. M., and Sawaya, R. (2002), “Necrosis and glioblastoma: a friend or a foe? A review and a hypothesis,” *Neurosurgery*, 51, 2–13.

- Rizzo, S., Botta, F., Raimondi, S., Origgi, D., Fanciullo, C., Morganti, A. G., and Bellomi, M. (2018), “Radiomics: the facts and the challenges of image analysis,” *European radiology experimental*, 2, 1–8.
- Robins, V., Saadatfar, M., Delgado-Friedrichs, O., and Sheppard, A. P. (2016), “Percolating length scales from topological persistence analysis of micro-CT images of porous materials,” *Water Resources Research*, 52, 315–329.
- Scarpace, L., Mikkelsen, L., Cha, T., Rao, S., Tekchandani, S., Gutman, S., and Pierce, D. (2016), “Radiology data from the cancer genome atlas glioblastoma multiforme [TCGA-GBM] collection,” *The Cancer Imaging Archive*, 11, 1.
- Scott, D. W. (2015), *Multivariate density estimation: theory, practice, and visualization*, John Wiley & Sons.
- Sefidgar, M., Soltani, M., Raahemifar, K., Bazmara, H., Nayinian, S. M. M., and Bazargan, M. (2014), “Effect of tumor shape, size, and tissue transport properties on drug delivery to solid tumors,” *Journal of biological engineering*, 8, 12.
- Siegel, R. L., Miller, K. D., and Jemal, A. (2020), “Cancer statistics, 2020,” *CA: A Cancer Journal for Clinicians*, 70, 7–30.
- Soltani, M. and Chen, P. (2012), “Effect of tumor shape and size on drug delivery to solid tumors,” *Journal of biological engineering*, 6, 4.
- Surawicz, T. S., McCarthy, B. J., Kupelian, V., Jukich, P. J., Bruner, J. M., and Davis, F. G. (1999), “Descriptive epidemiology of primary brain and CNS tumors: results from the Central Brain Tumor Registry of the United States, 1990-1994,” *Neuro-oncology*, 1, 14–25.
- Therneau, T. M. (2020), *A Package for Survival Analysis in R*, R package version 3.1-12.
- Turner, K., Mukherjee, S., and Boyer, D. M. (2014), “Persistent homology transform for modeling shapes and surfaces,” *Information and Inference: A Journal of the IMA*, 3, 310–344.

- Upadhyay, N. and Waldman, A. (2011), “Conventional MRI evaluation of gliomas,” *The British journal of radiology*, 84, S107–S111.
- Vogl, T. J., Worst, T. S., Naguib, N. N., Ackermann, H., Gruber-Rouh, T., and Nour-Eldin, N.-E. A. (2013), “Factors influencing local tumor control in patients with neoplastic pulmonary nodules treated with microwave ablation: a risk-factor analysis,” *American journal of roentgenology*, 200, 665–672.
- Wang, S., Chen, A., Yang, L., Cai, L., Xie, Y., Fujimoto, J., Gazdar, A., and Xiao, G. (2018), “Comprehensive analysis of lung cancer pathology images to discover tumor shape and boundary features that predict survival outcome,” *Scientific Reports*, 8, 10393.
- Wang, S., Yang, D. M., Rong, R., Zhan, X., and Xiao, G. (2019), “Pathology image analysis using segmentation deep learning algorithms,” *The American journal of pathology*, 189, 1686–1698.
- Yao, F., Müller, H.-G., and Wang, J.-L. (2005), “Functional Data Analysis for Sparse Longitudinal Data,” *Journal of the American Statistical Association*, 100, 577–590.
- Yokoyama, I., Sheahan, D., Carr, B., Kakizoe, S., Selby, R., Tzakis, A., Todo, S., Iwatsuki, S., and Starzl, T. (1991), “Clinicopathologic factors affecting patient survival and tumor recurrence after orthotopic liver transplantation for hepatocellular carcinoma,” *Transplantation Proceedings*, 23, 2194–2196.
- Zappa, C. and Mousa, S. A. (2016), “Non-small cell lung cancer: current treatment and future advances,” *Translational lung cancer research*, 5, 288.
- Zhang, C., Xiao, G., Moon, C., Chen, M., and Li, Q. (2020), “Bayesian Landmark-based Shape Analysis of Tumor Pathology Images,” *arXiv preprint arXiv:2012.01149*.
- Zhu, X., Li, K., Kamaly-Asl, I., Checkley, D., Tessier, J., Waterton, J., and Jackson, A. (2000), “Quantification of endothelial permeability, leakage space, and blood volume in brain tumors using combined T1 and T2\* contrast-enhanced dynamic MR imaging,” *Journal of Magnetic Resonance Imaging: An Official Journal of the International Society for Magnetic Resonance in Medicine*, 11, 575–585.

# Supplementary Material

## Introduction to Topological Data Analysis

### Homology with Toy Examples

Homology analyzes a shape with topological features in different spaces. Figure S1 presents three topological spaces and their Betti numbers. For example, the triangle in Figure S1b is one connected component with one hole ( $\beta_0 = 1$  and  $\beta_1 = 1$ ). Similarly, the Betti numbers of the circle in Figure S1b is  $\beta_0 = 1$  and  $\beta_1 = 1$ . Therefore, the Betti numbers of Figure S1b is two dimension-zero features and two dimension-one features ( $\beta_0 = 2$  and  $\beta_1 = 2$ ).

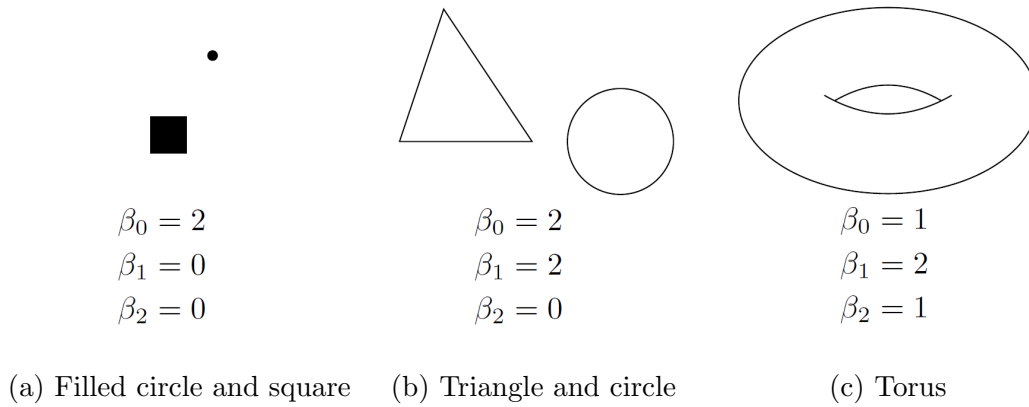
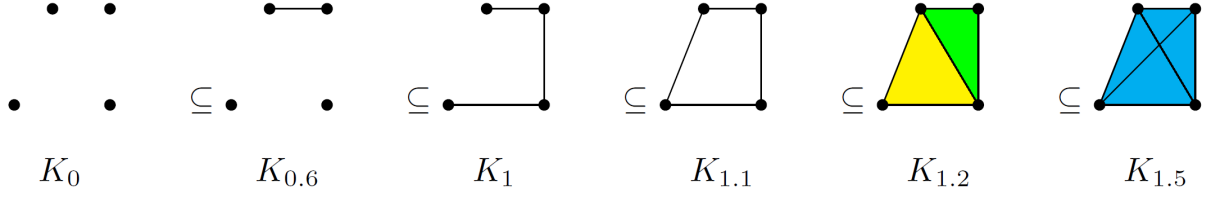


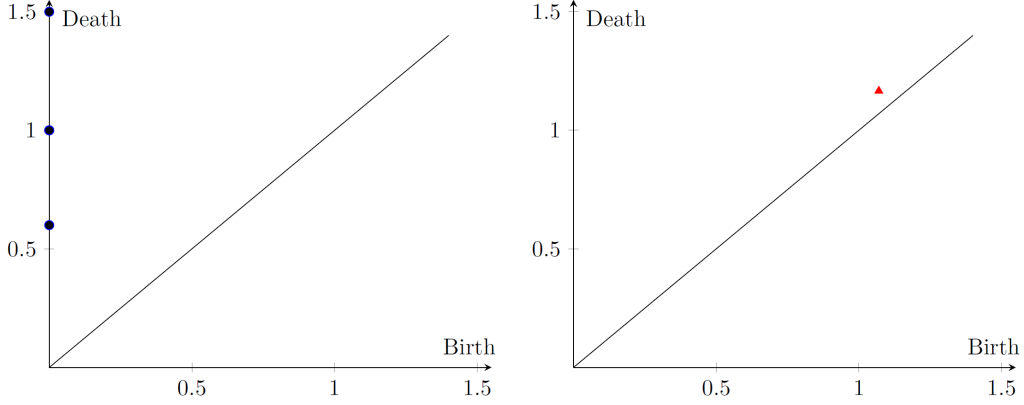
Figure S1: Topological space examples and their Betti numbers.  $\beta_0$ ,  $\beta_1$ , and  $\beta_2$  represent the number of zero-, one-, and two-dimensional holes.

### Persistent Homology with Toy Example

We explain persistent homology with a toy example to help understanding its concept. Figure S2a presents a sequence of simplicial complices,  $K_\epsilon$ , with four vertices at  $(0, 0)$ ,  $(1, 0)$ ,  $(1, 1)$ , and  $(0.4, 1)$ . In  $K_\epsilon$ , a  $(k - 1)$ -simplex is constructed if all pairwise distances between  $k$  vertices are less than or equal to  $\epsilon$ . We see that homology evolves as the filtration value  $\epsilon$  increases. For example, the 0-th Betti number of  $K_0$  is  $\beta_0 = 4$  as it has four disconnected points. On the other hand,  $\beta_0 = 3$  in  $K_{0.6}$  as the two points are connected.



(a) Sequence of simplicial complices



(b) Dimension-zero persistence diagram    (c) Dimension-one persistence diagram

Figure S2: (a): Sequence of simplicial complices and its persistent homology results summarized as dimension-zero and dimension-one persistence diagrams. In  $K_\epsilon$ ,  $k-1$ -simplex if all pairwise distances between  $k$  vertices are less than or equal to  $\epsilon$ . The dots and lines are vertices (0-simplices) and edges (1-simplices), respectively. The yellow- and green-colored regions in  $K_{1.2}$  are triangles (2-simplices), and the blue-colored region in  $K_{1.5}$  is a tetrahedron (3-simplex). (b)-(c): dimension-zero and dimension-one persistence diagrams of the simplicial complices (a).

Persistent homology observes the evolution of homology. For example, persistent homology computation output for  $0 \leq \epsilon \leq 1.5$  of Figure S2a is four intervals for dimension-zero,  $(0, 0.6)$ ,  $(0, 1)$ ,  $(0, 1)$ , and  $(0, 1.5)$ , and one interval for dimension-one,  $(\sqrt{1.16}, \sqrt{1.36})$ . The persistent homology computation results of Figure S2a can be illustrated as persistence diagrams in Figures S2b and S2c. Because the death of a topological feature comes after its birth, all points are placed above the diagonal line.

# Topological Shape Features by Persistent Homology Transform and Smooth Euler Curve Transform

The Persistent Homology Transform (PHT) is a recent addition to the topological shape analysis toolbox proposed by Turner et al. (2014). The PHT provides a detailed summary of shapes by sweeping their sub-level sets in different directions. For a shape in two- and three-dimensional spaces, a one-to-one relationship is guaranteed between the shapes and their PHT computation results (Turner et al., 2014). Consider a simplicial complex of interest  $K$  in  $\mathbb{R}^d$ . The sweeping direction  $\nu$  can be expressed as a point in a unit  $(d - 1)$ -sphere,  $\nu \in S^{d-1}$ . Let  $K_{(\nu, \epsilon)}$  be the sub-level complex that includes all simplices below the height  $\epsilon$  along the direction  $\nu$ . For a given direction and orientation, persistent homology is computed using the height as a filtration,  $h_{\min} \leq \epsilon \leq h_{\max}$ , where  $h_{\min}$  and  $h_{\max}$  are range of filtration that can include all simplices in  $K_{(\nu, \epsilon)}$ . The process is repeated over infinitely many directions in  $S^{d-1}$  and the shape is summarized as a collection of persistence diagrams. In real applications, a large enough number of directions are selected. PHT can be defined as a function  $\text{PHT}(K) : S^{d-1} \rightarrow \mathcal{D}^d$ .

The Euler Characteristic Transform (ECT) is a simple extension of the PHT. The Euler characteristic is a commonly used value to examine the topological properties as a single integer. The Euler characteristic of topological space  $\mathcal{S}$  is  $\chi(\mathcal{S}) = \beta_0 - \beta_1 + \beta_2 + \dots = \sum_{i=0}^{\infty} (-1)^i \beta_i$ , where  $\beta_i$  is  $i$ -th Betti number of  $\mathcal{S}$ . The ECT generates a set of Euler characteristic curves, similar to a set of persistence diagrams in the PHT. We denote  $\chi(K_{(\nu, \epsilon)}) \in \mathbb{Z}$  as the Euler characteristic curve that tracks evolution of the Euler characteristic for a given sweeping direction  $\nu$ , orientation, and the filtration from  $h_{\min}$  to  $h_{\max}$ . The ECT collects the Euler characteristic curve from all directions and can be defined as a function  $\text{ECT}(K) : S^{d-1} \rightarrow \mathbb{Z}^{\mathbb{R}}$ . Because the Euler characteristic is the alternating sum of the rank of the homology group, the ECT is also an injective function. Crawford et al. (2020) propose the Smooth Euler Characteristic Transform (SECT) that computes the centered and cumulative Euler characteristic curve by subtracting the mean from the Euler characteristic curve,  $\chi(K_{(\nu, \epsilon)}) - \bar{\chi}(K_{(\nu, \epsilon)})$ . The SECT collects a set of functions in Hilbert space,  $\text{SECT}(K) : S^{d-1} \rightarrow \mathbb{L}^2[h_{\min}, h_{\max}]$ .



# Persistent Homology for Multi-class Medical Images

## Persistent Homology Computation

We illustrate the proposed persistent homology approach for medical images with the three-class tumor image example. First, Figure S3a presents the three-class example image where the green-, blue-, and yellow-colored pixels are tumor, normal, and empty regions, respectively. Figure S3b shows the signed distance transformed values assigned for each pixel. Here, a taxicab metric is used instead of a Euclidean distance for convenience.

We construct cubical complices using the signed distance. Let  $\mathcal{C}_\epsilon$  be the cubical complex with filtration  $\epsilon$ . In  $\mathcal{C}_\epsilon$ , the pixels whose assigned distances are less than  $\epsilon$  enter the complex. Figures from S3c to S3h in Supplementary Material present the sequence of cubical complices with  $\epsilon \in \{-3, -2, \dots, 3\}$ .

In Figure S3 example, two dimension-zero features (i.e., connected components) are recorded. The first dimension-zero feature appears in  $\mathcal{C}_{-3}$  in the bottom-left corner of Figure S3c and the second dimension-zero feature is created in  $\mathcal{C}_{-1}$  in the middle of Figure S3e. Two components are connected in  $\mathcal{C}_1$  so the second feature dies at  $\epsilon = 1$ . Also, we observe three dimension-one features (i.e., loops) in the example. Two holes show up in  $\mathcal{C}_{-1}$  in the middle of Figure S3e. The smaller hole disappears in  $\mathcal{C}_1$  and the larger hole is filled in  $\mathcal{C}_2$ . The other dimension-one component appears in  $\mathcal{C}_1$  and disappears in  $\mathcal{C}_2$ .

The birth and death information of topological features explained above is summarized in persistent diagrams in Figures S3i and S3j.

## Interpretation of Persistent Homology Computation Result

Persistent homology computation results summarize various tumor shape patterns. Dimension-zero features appear in the three non-zero quadrants of persistence diagrams: 1) quadrant II (e.g., A, B, C, and D of Figure 2 in the main article); 2) quadrant I (e.g., E and F of Figure 2 in the main article); and 3) and quadrant III (e.g., G, H, and I of Figure 2 in the main article). First, the scattered tumors are recorded in quadrant II. The larger the tumor regions, the larger birth values are in quadrant II (e.g., A vs. B and C vs. D of Figure 2 in the main article). Also, larger death values imply that distances between the disconnected

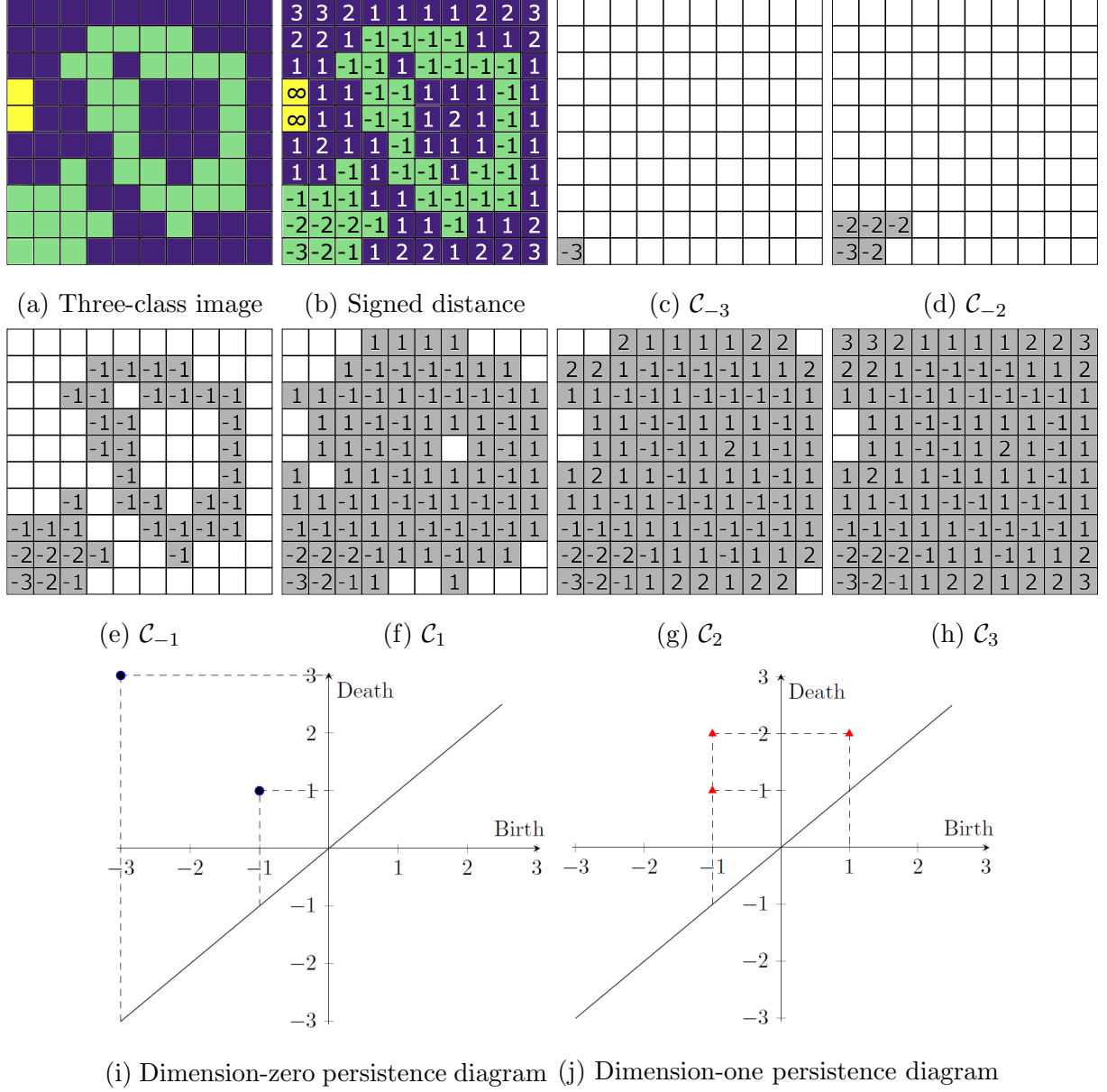


Figure S3: (a): Three-class example image. The green-, blue-, and yellow-colored pixels are tumor, normal, and empty regions, respectively. (b): Signed distances using the taxicab distance. (c)-(h): a sequence of cubical complices based on the computed signed distance. The pixels included in the cubical complices are marked in gray. (i)-(j): dimension zero- and one-persistence diagrams.

tumor regions are far from each other (e.g., A vs. C and B vs. D of Figure 2 in the main article). Second, quadrant I represents the separate normal regions that include tumor

regions. Death values are proportional to the distance between the boundary of normal regions and the tumor regions inside (e.g., E vs. F of Figure 2 in the main article). Third, connected tumor regions appear in quadrant III. The birth values are the size of tumor regions (e.g., G vs. H of Figure 2 in the main article), and the death values are the size of the contact area of two tumor regions (e.g., G vs. I of Figure 2 in the main article). The death value illustrates how close the tumor regions are. The connected tumor regions can be in different shapes. For example, they could be a series of overlapped tumor regions (left figures of G, H, and I of Figure 2 in the main article) or tumor regions that have normal regions inside (right figures of G, H, and I of Figure 2 in the main article).

Dimension-one features are summarized in two quadrants: 1) quadrant II (e.g., J, K, L, and M of Figure 2 in the main article); and 2) quadrant I (e.g., N, O, and P of Figure 2 in the main article). First, the normal regions surrounded by the tumor regions appear in quadrant II. Here, the large negative birth value means the surrounding tumor regions are thick (e.g., J vs. K and L vs. M of Figure 2 in the main article), and the large death value means the trapped normal regions are large (e.g., J vs. L and K vs. M of Figure 2 in the main article). Second, the broken-ring-shaped or double-broken-ring-shaped tumor regions are recorded in quadrant I. The large birth values imply that there are large gaps in the broken-ring or double-broken-ring-shaped shaped regions (e.g., N vs. O of Figure 2 in the main article). Also, the large death value means the size of the inside of the broken-ring or double-broken-ring shape is large (e.g., N vs. P of Figure 2 in the main article).

## Validation Test Results

We examine the validity of topological features in the Functional Cox Proportional Hazards model (FCoxPH) for predicting the survival outcome. We conduct the chi-square test with  $q + r$  degrees of freedom that uses the  $q + r$  number of coefficients of functional basis,

$$H_0 : \quad \alpha_1 = \alpha_2 = \dots = \alpha_q = \beta_1 = \dots = \beta_r = 0$$

$$H_1 : \quad \alpha_j \neq 0 \text{ or } \beta_k \neq 0 \text{ for at least one } j \in \{1, 2, \dots, q\} \text{ or } k \in \{1, 2, \dots, r\}.$$

As suggested in Kong et al. (2018), we use the percentage of variance explained by the functional principal components (FPCs) to select  $q$  and  $r$ .

### Lung Cancer Pathology Image Application

For the lung cancer pathology images, we use the variance threshold  $C = 90\%$  and three dimension-zero and two dimension-one functional basis are selected ( $q = 2$  and  $r = 3$ ). For the proposed FCoxPH model of pathology images, we conduct the chi-square test of degrees of freedom five. The computed p-value is  $1 \times 10^{-13}$ , suggesting that the topological features are a strong signal. Aside from the clinical variables included in the model, the topological features offer additional information in predicting lung cancer patients' survival outcomes.

### Brain Tumor MRI Image Application

We conduct the chi-square test to examine validity of functional topological shape features obtained from the brain tumor MRI images. We use the variability threshold  $C = 90\%$  and four dimension-zero and four dimension-one FPCs are selected ( $q = r = 4$ ), respectively. The p-value of the chi-square test of degrees of freedom of eight is  $2 \times 10^{-4}$ . This implies that the proposed topological shape features are informative for predicting the survival outcomes of the glioblastoma multiforme patients after adjusting the clinical variables.